Contents lists available at ScienceDirect

Applied Thermal Engineering

journal homepage: www.elsevier.com/locate/apthermeng

Research Paper

Visualization study on operating performance of a dual compensation chamber loop heat pipe under acceleration condition

Yongqi Xie [a],[*], Zhen Fang [a], Hongxing Zhang [b], Hongwei Wu [c],[**], Siyuan Liu [a]

[a] School of Aeronautic Science and Engineering, Beihang University, Beijing 100191, China
[b] Beijing Key Laboratory of Space Thermal Control Technology, China Academy of Space Technology, Beijing 100094, China
[c] School of Physics, Engineering and Computer Science, University of Hertfordshire, Hatfield AL10 9AB, UK

ARTICLE INFO

ABSTRACT

In this article, a novel visual dual compensation chamber loop heat pipe (DCCLHP) under acceleration conditions was experimentally investigated. The working fluid was deionized water and the wick material was sintered nickel powder. Visual windows were installed on both compensation chambers (CCs) and condenser in order to observe the vapor and liquid distribution. The operating performance and physical mechanism of the proposed DCCLHP under both acceleration direction A and B at different heat loads and acceleration magnitudes were analysed in a systematic manner. Direction A refers the acceleration direction which was parallel to the axis of the evaporator and the CC without a bayonet placed at the outer edge of the rotating arm. While direction B is defined as the acceleration direction was perpendicular to the axis of the evaporator and the evaporator was placed at the outer edge of the rotating arm. In the current study, the heat load varies from 30 W to 130 W and the acceleration magnitude ranges from 1 g to 15 g. Experimental results revealed that: (i) The larger the heat load, the higher the operating temperature. Obviously waving of the vapor-liquid interface in the CC is observed at direction A. Bubbles generated in the CCs and the vapor-liquid interface moves back and forth in the condenser during temperature oscillation at both 70 W and 90 W for the case of 13 g and direction B. (ii) Under direction B, the DCCLHP presents lower operating temperature and higher thermal conductance. The maximum temperature is 143.2 °C at 5 g and 90 W under direction A. The maximum thermal conductance is 1.70 W/K at 13 g and 130 W under direction B. (iii) In general, the operating temperature shows a trend of decreasing first and then increasing with the increase of acceleration. Whereas the thermal conductance shows an opposite behavior. The transition acceleration, namely the acceleration magnitude at the minimum temperature, is 13 g for the case of direction A. However, under direction B, the large heat load can result in a large transition acceleration. (iv) Intermittent spattering of liquid drops is observed in the CCs at 70 W and 15 g under direction A. The flow pattern under direction A is different with that under direction B at each heat load. Multiple segments of the liquid and vapor phase alternately distribute and stratified flow forms in the condenser.

1. Introduction

With continuous performance improvement of advanced flight vehicle, a large number of electronic equipment with higher power dissipation and larger heat flux have been utilized within a limited airborne space. It has been realized that traditional air cooling and liquid cooling technology cannot meet such high heat dissipation requirement. It is therefore imperative to develop an efficient and compact phase change cooling technology [1,2]. Loop heat pipe (LHP), as an efficient two-phase heat transfer device, exploits the capillary force generated by the wick to drive the working fluid to cycle and transport the heat by the phase change latent heat of the working fluid. LHP has now attracted extensive attention in the cooling of electronic equipment, battery thermal management and aircraft environment control due to its advantages such as large and long-distance heat transfer, high efficiency, without external power and flexible installation [3–7].

In the terrestrial gravity environment, the LHP with a single compensation chamber (CC) could face challenges of being unable to startup and operate normally due to the liquid working fluid is not able to supply the primary wick for the condition of the evaporator above the CC [8,9]. For flight vehicles such as aircraft and missile, they always

---

Nomenclature

a	acceleration [m/s^2]
$D_{W,I}$, $D_{W,O}$	Inner diameter and outer diameter of wick [m]
g	Gravitational acceleration [9.81 m/s^2]
G	Thermal conductance [W/K]
I	Current A
k	Thermal conductivity coefficient [W/(m·K)]
L	Length [m]
m	Mass flow rate [kg/s]
Δp	Pressure drop [Pa]
$\Delta p_{CON}^{2\varphi}$, $\Delta p_{CON}^{1\varphi}$	Pressure drop of two-phase fluid and single-phase fluid in the condenser [Pa]
Q	Heat load [W]
t	time s
T	Temperature [K]
V	Voltage V
$(dp/dT)_{SAT}$	Slope of saturation curve [Pa/K]
$\triangle T$	Temperature difference [K]
x	Independent variable

Greek symbols

γ	Latent heat of the evaporation [J/kg]
ρ	Density [kg/m^3]

Subscripts

a	Acceleration
A	Axial
AM	Ambient
B	Bayonet
EVA	Evaporator
EVA-CC	Between evaporator and compensation chamber
HL	Heat leak
IN	At inlet
OUT	At outlet
R	Radial
S	Heat sink
SC	Subcooling
VG	Vapor groove
W	Wick

Acronyms

CC	Compensation chamber
DCCLHP	Dual compensation chamber loop heat pipe
EPDM	Ethylene propylene diene monomer
ID	Inner diameter
LHP	Loop heat pipe
OD	Outer diameter

suffer from the elevated acceleration environment during maneuvering flight. When the single CC LHP is used to cool the airborne electronic equipment, the problem that the liquid cannot supply the primary wick will be more prominent under the elevated acceleration force. The effect of the acceleration force can even make the single CC LHP fail to operate properly and further cause the damage of electronic equipment due to overheating [10–12]. Therefore, based on the single CC LHP, LHP with two CCs on the two ends of the evaporator, that is dual compensation chamber loop heat pipe (DCCLHP), was developed to achieve the liquid working fluid supply for the primary wick under any orientation in terrestrial gravity [13,14]. It has been proved that the DCCLHP could operate successfully at any orientation in the terrestrial gravity [15–18] and in the acceleration field [19,20].

When LHP operates properly, vapor-liquid two-phase fluid will occupy the evaporator, compensation chamber and condenser. The operating performance and heat transfer mechanism of the LHP depends crucially on the vapor-liquid distribution and phase change of the working fluid in the above three components. Nowadays, much efforts has been devoted to experimental work [15,16,21–24], numerical simulation [25–28] and theoretical modeling [29–32] on LHP. However, the physical mechanism of LHP is not well understood and there is still much room to be investigated further. It is noted that although the operating performance can be assessed by the external wall temperature of the loop [21,33–35], some phenomena such as boiling in the core cannot be addressed reasonably due to lack of visualization of internal flow and heat transfer behaviors of the loop. Therefore, visualization study on the LHP is extremely necessary in order to reveal the operating mechanism from different angle.

For the visualization study on the LHP, neutron radiography, transparent or translucent materials such as high-strength glass and PTFE are normally used to observe the two-phase flow and phase distribution inside the loop. Cimbala et al. [36,37] experimentally studied the operating performance of a single CC LHP by neutron radiography. They revealed that slugs of vapor were sometimes observed in the liquid line and slugs of liquid were observed in the vapor line during transient periods. Moreover, partial wick dryout under certain conditions could be observed by neuron imaging. Okamoto et al. [38,39] presented the visualization of a single CC LHP using neutron radiography. It was found

that the LHP failed to start up at the heat load of 120 W. The middle of the primary wick would dryout and the dryout area expanded with time, which caused the evaporator temperature to continually increase. Zhang et al. [40] studied experimentally enhancement effect of groove structure on boiling heat transfer in a flat LHP with visual evaporator. The results presented that the degree of nucleate boiling in the inner region of heating section was more intense than that near the case. Lin et al. [41] experimentally investigated the startup and steady-state performance of a DCCLHP with visual CCs and condenser under gravity field. It was observed that the bubble generation in the evaporator core, reverse flow, fluctuated flow and liquid redistribution occurred. The main reason was the radial heat leak from the evaporator. Wang et al. [42] investigated the start-up characteristics of a new type of LHP under different conditions. It was found that the system started faster with the increase of heat load, and the peak temperature decreased obviously, and more intense boiling phenomenon appears in the CC. Yang et al. [43] designed a visual flat LHP and obtained the operating performance inside of the evaporation chamber. They found that the circulation driven head inside of the evaporation chamber can significantly promote the operating characteristics. For the purpose of application to aircraft anti-icing, Chang et al. [44,45] designed a DCCLHP using ethanol–water mixture as working fluid to evaluate the performance of the wing anti-icing. Nishikawara et al. [46] fabricated a quartz wick-acetone LHP with a transparent glass evaporator wall. They observed the nucleate boiling occurred in the wick or groove. The different vapor–liquid phase distributions brought the different temperature profile during the process of start-up. Yamada et al. [47] carried out a visualization experiment for the quartz wick-acetone LHP with a glass tube evaporator. Their results demonstrated two vapor–liquid phase states at the case-wick contact surface. Zhang et al. [48] developed a half-sectioned cylindrical structure evaporator-CC sealed with a glass window. The flow and heat transfer performance in the evaporator-CC was visually investigated at different heat loads and tilt angles. It was found that the vapor–liquid interface changed with the variation of heat load. The interface oscillation led to the temperature oscillation in the evaporator core.

In addition to the evaporator and/or CC, the researchers also visualized the two-phase condensation process in the condenser. Achkar

et al. [49] studied the heat transfer in the isolated bubble region in the S-shaped glass microchannel condenser of the LHP. Bartuli et al. [50] visualized the process of condensation and redistribution of working fluid in LHP and observed stratified two-phase flow and film condensation under all working conditions. Chang et al. [51,52] used cameras to observe the heat transfer process of the working fluid in two evaporators and one condenser. The two-phase flow region and heat leak ratio in the gravity-assisted mode were longer and smaller than those in the capillary-gravity driving mode. Based on the bubble tracking and image processing method, Zhou et al. [53] designed a LHP with transparent evaporator and condenser, and studied the characteristics of two-phase flow under gravity-assisted condition. The operating temperature under different heat loads and the two-phase flow patterns of the start-up phase and the steady-state phase were determined. For a propylene cryogenic LHP with a visual condenser, Yan et al. [54,55] clearly observed two-phase flow patterns at the temperatures between 153 and 283 K, including stratified flow, slug flow, pseudo-slug flow and wavy-annular flow.

The above visualization investigations on the LHP provide a theoretical support for improving the flow and heat transfer mechanism. However, most of the previous studies mainly focused on the operating performance of LHP under terrestrial gravity. There are quite few experimental and theoretical studies on LHP characteristics under elevated acceleration fields and only several open published literatures have been reported. Ku et al. [56,57] experimentally studied the effect of acceleration magnitude, direction, frequency and heat load on the start-up and operating performance of the LHP with a single CC. The acceleration varies from 1.2g to 4.8g. It was confirmed that the superheat and temperature overshoot appeared to be independent on the acceleration force. The fluid distribution in the evaporator, condenser and CC can be impacted by acceleration effect, which further changed the operating temperature. The operating performance of a titanium-water LHP with a single CC was studied by Fleming et al. [11] under gravity and elevated acceleration fields. It was revealed that the dry out was a function of both heat load and radial acceleration. The evaporator wall superheat increased slightly with the increase of acceleration at high heat load. Yerkes et al. [58] also experimentally investigated the transient operating performance of a titanium-water LHP subjected to a steady-periodic acceleration force in the form of a sine wave. They stated that the acceleration effect sometimes can improve or deteriorate the LHP dynamical performance. In addition, the immediate or delayed failure of LHP to operate can be caused as acceleration force countered thermodynamic force. They [59] further studied the operating performance of a titanium-water LHP subjected to a phase-coupled heat load from 100 W to 700 W and radial acceleration from 3 g to 10 g. It was confirmed that the LHP failed to operate when the heat load and acceleration had different phase angle. For a stainless steel-ammonia DCCLHP, the authors [60–62] experimentally investigated the start-up and steady-state performance under acceleration field. Their results indicated that the acceleration effect can alter the loop pressure drop and two-phase flow and heat transfer behaviors, and further led to a unique operating performance. Nevertheless, the explanation of some phenomena in elevated acceleration environment was based on assumptions for the flow and heat transfer in the loop due to lack of direct observation.

It is recognized that the theory of two-phase flow and heat transfer of LHP has been gradually improved with the aid of visualization study under terrestrial gravity. However, to the best of authors' knowledge, there is still lack of systematic research on the operation characteristics and heat transfer mechanism of LHP under complex acceleration fields. Especially the visualization study on the DCCLHP subjected to acceleration force have not been investigated. Therefore, the current work aims to visually observing the two-phase flow and heat transfer behavior in the DCCLHP under acceleration fields. Another major contribution is to explore the operating characteristics of the DCCLHP under different acceleration magnitudes, directions and heat loads. According to the

observation on the flow and heat transfer behaviors of the working fluid in CCs and condenser, the operating mechanism of the DCCLHP in the acceleration environment can be addressed thoroughly. In the current work, a visual DCCLHP will be designed and fabricated. The effects of heat load, acceleration magnitude and direction on the operating performance of the DCCLHP will be analyzed in a systematic manner. Moreover, the vapor–liquid phase distribution and the flow pattern in the condenser and CCs will be observed and the operating mechanism will be discussed.

2. Experimental apparatus and procedure

2.1. Visual LHP design

In the current work, a nickel-water DCCLHP with visual window was designed and fabricated, as shown in Fig. 1. The system mainly consists of evaporator, CCs, condenser and vapor and liquid transport line. Two CCs were arranged at both ends of the evaporator to guarantee that the wick can be submerged by the liquid working fluid at any orientation. The internal structure of the evaporator and CCs is presented in Fig. 1(a). Two borosilicate glass windows were installed on both sides of each CC, as shown in Fig. 1(b). Ethylene propylene diene monomer (EPDM) gasket seal was adopted between the threaded end, glass windows and the shell of the CC. The wick with average pore diameter of 1.1 μm was sintered from micron-sized nickel powders. Vapor channels with 177 mm (length) × 1.0 mm (width) × 1.0 mm (height) was manufactured on the outside of the wick, as shown in Fig. 1(c). The vapor from the liquid evaporation was collected and sent to the vapor collecting chamber. The specific parameters of DCCLHP are listed in Table 1.
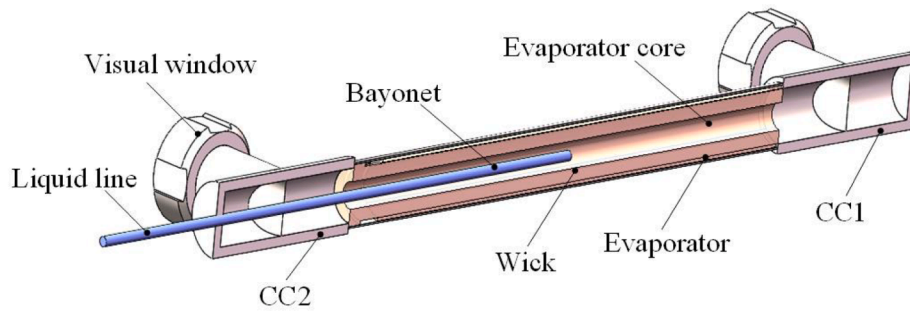
The condenser of the DCCLHP was composed of the cover plate, glass window and base plate. Serpentine channel with rectangular section was milled on the copper base plate. The size of the channel was 3 mm in width, 3 mm in height and 1000 mm in length. In order to observe the flow of the working fluid inside the condenser, the borosilicate glass window was used to cover the serpentine channel. Sealing grooves with a width of 1.5 mm were also manufactured on both sides of the channel to avoid the cross flow of the working fluid by placing the EPDM strip. Finally, the cover plate, the screws and the EPDM gasket were used to compress the glass window and seal the channel, as shown in Fig. 1(d).

The working fluid such as water, ethanol and acetone has the low vapor pressure. Moreover, the water has the largest latent heat of evaporation and is a widely used working fluid [63–65]. In the current visualization study, deionized water was selected as the working fluid.

2.2. Experimental setup

Fig. 2 presents a schematic diagram of the DCCLHP visual test rig. The system mainly includes the recirculating water cooling system, the heating control and data acquisition system, the acceleration simulation system, and the visual test section. The recirculating water cooling system is composed of a thermostatic water tank (Sanffo HK-30/20L), a magnetic pump, a mass flow meter (DMF-1-2), a regulating valve and an aluminum cold plate (type 6061), which provides cooling water for the condenser of the DCCLHP. The heating control and data acquisition system is composed of a DC power supply, an electric heating film, an Agilent data acquisition instrument, pt100 temperature sensors, junction boxes and a remote computer. It can heat the evaporator and record the temperature of the DCCLHP. The acceleration simulation system consists of a Y53100-3/ZF centrifuge, transducer controller and computer controller. It simulates the required acceleration environment.

As shown in Fig. 2, the visual test section was horizontally installed on the rotating arm of the centrifuge. The visual condenser of the DCCLHP was mounted on the upper surface of the cold plate of the recirculating water cooling system. Thermal conductive grease was used between the condenser and the cold plate to decrease the contact thermal resistance. The heat from the evaporator was transported to the

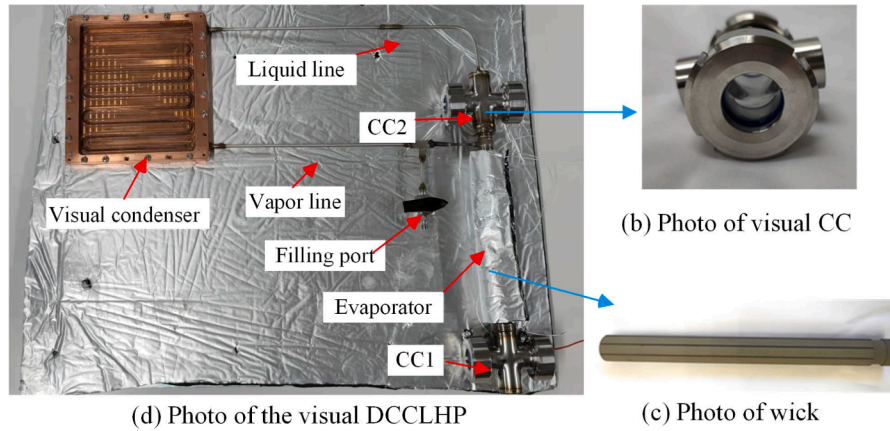(a) The internal structure of the evaporator and CC

(b) Photo of visual CC

(d) Photo of the visual DCCLHP

(c) Photo of wick

Fig. 1. The internal structure of the evaporator and CCs and photo of Visual DCCLHP.

Table 1
Specific parameters of DCCLHP.

Components	Material	Parameter	Dimensions
Evaporator	Stainless steel 316L	OD/ID/Length (mm)	20/18/210
		OD/ID/Length (mm)	18/8/189.5
Wick	Nickel	Porosity	48.5 %
		Permeability (m^2)	1.3×10^{-14}
		Pore radius (μm)	1.1
CCs	Stainless steel 316L	Volume (ml)	50
Vapor line	Stainless steel 316L	OD/ID/Length (mm)	3/2/300
Liquid line	Stainless steel 316L	OD/ID/Length (mm)	3/2/380
Condenser	Stainless steel 316L	Width/Height/Length (mm)	3/3/1000

cooling water by the cold plate. The water absorbing the heat recycled back to the thermostatic water tank. In order to reduce the heat exchange with the surroundings, all the DCCLHP was wrapped with insulation materials except visual windows and fixed in a stainless-steel enclosure, which was also covered with aluminum foil insulation materials. In the enclosure, two video cameras fixed the frame to 60 fps and the video frame to 2704 × 1520 pixels for the condenser and both CCs. Two LED lights were used as fill-in flash for the cameras, as shown in Fig. 3(a).

2.3. Experimental conditions and procedure

In the current work, all test cases are listed in Table 2. Five radial acceleration magnitudes (1 g, 5 g, 9 g, 13 g and 15 g) and two acceleration directions (namely directions A and B) were studied. For direction A, the radial acceleration direction was consistent with the axis of the evaporator and pointed CC1 from CC2. While for direction B, the radial acceleration direction was perpendicular to the axis of the evaporator and the evaporator was placed at the outer edge of the rotating arm. The schematic diagram of both directions A and B was shown in

Fig. 3(a). The local coordinate system was defined in Fig. 3(a). The direction of the gravity was along the negative direction of the Z axis. The acceleration direction A and B were along the positive direction of the X and Y axis, respectively. The photo of DCCLHP installed in tooling is seen in Fig. 3(b).

Different heat loads on the evaporator were employed for the cases of direction A and B. It is noted that due to different direction, acceleration effects could change the maximum heat load of the DCCLHP when operating normally. The heat load for direction A was 30 W, 40 W, 50 W, 60 W, 70 W, 80 W and 90 W, whereas for direction B was 30 W, 50 W, 70 W, 90 W, 110 W and 130 W. During the experiment, the acceleration force and heat load were applied simultaneously. The maximum continuous working time of the centrifuge was 1 h for the purpose of safety. The inlet cooling water temperature of the cold plate was maintained ranging from 20 °C to 22 °C. The room temperature was kept from 25 °C to 26 °C.

The locations of the total eleven temperature monitoring points along the loop are shown schematically in Fig. 3(a). CC1_T and CC1_B were attached on the top and bottom of the CC1 outer surface. While CC2_T and CC2_B were attached on the top and bottom of the CC2 outer surface, respectively. EVA was located at the middle point of the evaporator surface. VL was attached near the middle of the vapor line. CON1 and CON2 were used to monitor the temperature of the condenser surface. LL_OUT was located on the outer surface of the liquid line near the outlet. COLD_IN and COLD_OUT were used to measure the inlet and outlet temperatures of the cooling water for the condenser.

2.4. Hydrodynamic and thermodynamic analysis

When the DCCLHP operates normally, the capillary pressure generated by the wick must be not less than the total pressure drop of the external loop Δp_{total}, which can be calculated by Eq. (1):
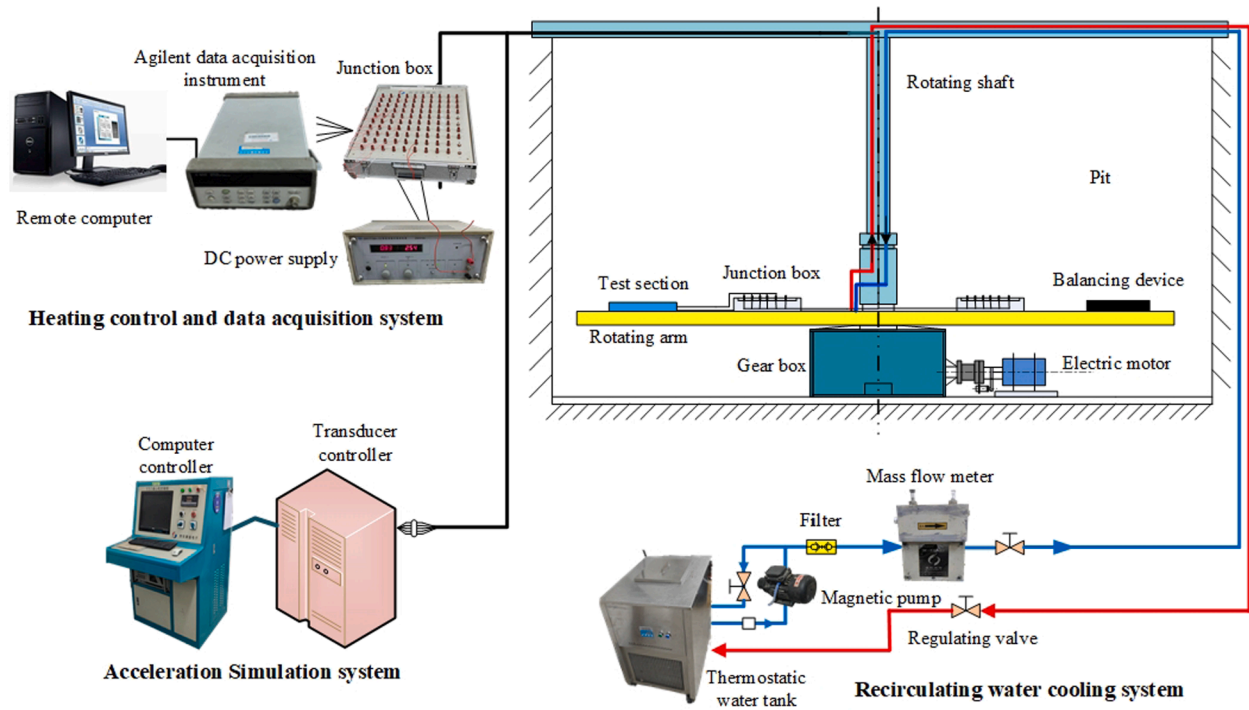
Fig. 2. Schematic diagram of the DCCLHP visual test rig.

$$\Delta p_{\text{total}} = \Delta p_{\text{VG}} + \Delta p_{\text{VL}} + \Delta p_{\text{CON}}^{2\varphi} + \Delta p_{\text{CON}}^{1\varphi} + \Delta p_{\text{LL}} + \Delta p_{\text{B}} + \Delta p_{\text{W}} + \Delta p_{\text{a}} \qquad (1)$$

In Eq. (1), the value of each term except for the last term Δp_{a} depend on the mass flow rate of the working fluid. The additional pressure resulted from the acceleration force Δp_{a} depends on the length of liquid column along with the acceleration, which can be determined by Eq. (2).

$$\Delta p_{\text{a}} = \rho a L \qquad (2)$$

When the acceleration direction was the same as the flow direction of the working fluid, the additional pressure played a driven force. While if the acceleration direction was opposite to the flow direction, the additional pressure became a flow resistance.

Assuming that the working fluid was saturated liquid in the wick and was saturated vapor as leaving the evaporator, the heat load on the evaporator except for the heat leak from evaporator to CC was absorbed by the working fluid in form of heat latent. The mass flow rate can be determined by Eq. (3).

$$m = (Q_{EVA} - Q_{HL})/\gamma \qquad (3)$$

The heat load on the evaporator can be determined by Eq. (4), which is the product of the voltage and the current through the electric heating film.

$$Q_{EVA} = VI \qquad (4)$$

The heat leak included the radial and axis heat leak. It can be calculated by Eq. (5).

$$Q_{HL} = Q_{HL,R} + Q_{HL,A} = \frac{2\pi k_W L_W}{\ln\left(D_{W,O}/D_{W,I}\right)}\Delta T_W + k_{\text{EVA-CC}} A_{\text{EVA-CC}} \frac{T_{\text{EVA}} - T_{\text{CC}}}{L_{\text{EVA-CC}}} \qquad (5)$$

At a steady state, the heat leak from the evaporator to the CC can be balanced by the subcooling of the returning liquid and the heat leak from the CC to the ambient. Considering the energy balance relationship of the CCs, the following Eq. (6) was true.

$$Q_{HL} = Q_{AM} + Q_{SC} \qquad (6)$$

In addition, the temperature difference between the evaporator and

the CC $\triangle T_{\text{EVA-CC}}$ can be determined by the pressure difference between the evaporator and the CC $\triangle p_{\text{EVA-CC}}$ according to the Clausius-Clapeyron relation:

$$\Delta p_{\text{EVA-CC}} = (dp/dT)_{\text{SAT}} \Delta T_{\text{EVA-CC}} \qquad (7)$$

In the current work, the evaporator temperature was used as the operating temperature of the DCCLHP.

2.5. Uncertainty analysis

If the variable X is calculated by the independent variables ($x_1, x_2, \ldots, x_n$), the uncertainty of X can be expressed as [66]:

$$\delta X = \left[\sum_{i=1}^{n} \left(\frac{\partial X}{\partial x_i} \delta x_i \right)^2 \right]^{1/2} \qquad (8)$$

where δx_i is the uncertainty of the x_i.

The thermal conductance G of the DCCLHP was determined by the following expression:

$$G = \frac{Q_{\text{EVA}}}{T_{\text{EVA}} - T_{\text{S}}} \qquad (9)$$

where Q_{EVA} is the heat load on the evaporator, T_{EVA} is the evaporator temperature, and T_{S} is the average temperature of the cold plate determined by $T_{\text{S}} = (T_{\text{IN}} + T_{\text{OUT}})/2$.

The temperature of the loop was a direct measurement value. The temperature measurement accuracy was about $\pm$ 0.5 °C and the maximum temperature uncertainty was 3.31 % due to the impact of the electric wire, junction terminate, slip ring, data logger and temperature sensor. For the voltage and the current, the maximum uncertainty was 0.62 % and 2.63 % respectively. Thus, the maximum uncertainty was 2.66 % for the heat load. For the thermal conductance, the maximum uncertainty was 3.02 % according to Eq. (9). In summary, the uncertainty analysis results of each parameter are shown in Table 3.
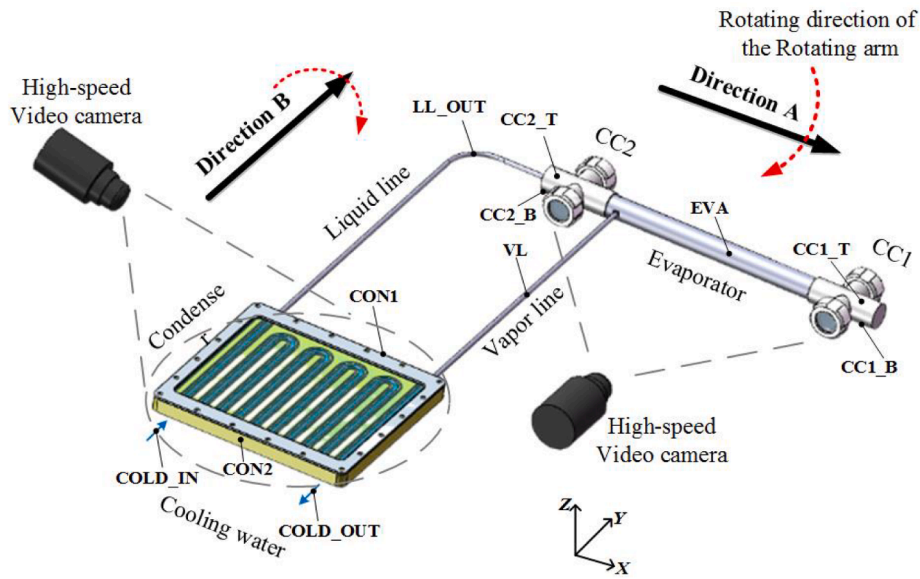
(a) Schematic diagram
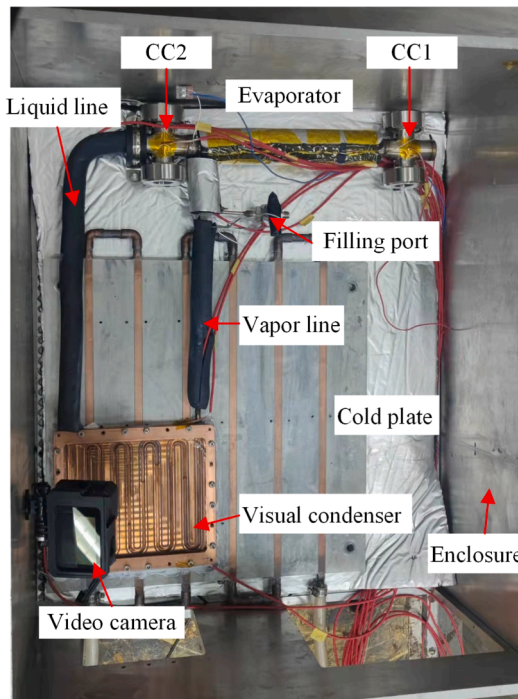
(b) Test section picture

Fig. 3. Picture of acceleration directions of A and B and temperature monitoring points.

Table 2
Test cases.

Parameter	Variation
Acceleration	1 g, 5 g, 9 g, 13 g, 15 g
Acceleration direction	A, B
Heat load (W)	30, 40, 50, 60, 70, 80, 90 (A)
	30, 50, 70, 90, 110, 130 (B)

Table 3
Uncertainty analysis results.

Variable	Temperature	Voltage	Current	Heat load	Thermal conductance
Uncertainty	3.31 %	0.62 %	2.63 %	2.66 %	3.02 %

3. Results and discussion

3.1. Effect of heat loads

Fig. 4 presents the temperature profile of the DCCLHP under direction A and 1 g at different heat loads of 30 W, 50 W and 70 W. It can be clearly seen from Fig. 4 that the evaporator temperature was significantly higher than that of vapor line and the other components. The evaporator temperature increased progressively along with the increase of heat load. The CC1_T and CC1_B temperature of the CC1 was almost unchanged and obviously less than the temperature of the CC2. The
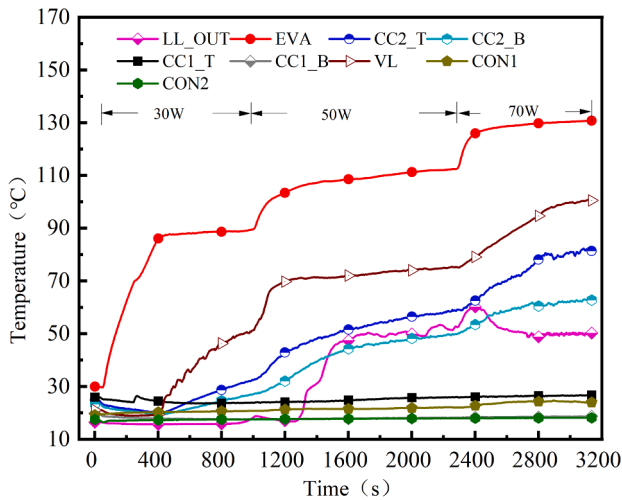
Fig. 4. Temperature curves of the DCCLHP at 1 g and direction A for 30 W, 50 W and 70 W.

LL_OUT temperature of the liquid line at 50 W and 70 W was significantly higher than that at 30 W.

During the initial period of the heat load of 30 W, the evaporator temperature firstly went up rapidly. While it is after approximate 320 s that the VL temperature started to rise. It shows that the vapor derived from the evaporator reached to the VL temperature monitoring point. The DCCLHP could be deemed start-up. The CC2_T and CC2_B temperature raised progressively following the VL temperature. The final operating temperature of the DCCLHP, which is the evaporator temperature at 30 W was 89.4 °C. When the heat load increased to 50 W, the evaporator temperature raised rapidly. It is at about 1290 s that the LL_OUT temperature of the liquid line suddenly increased until it reached approximate 52 °C during the heat load of 50 W. The LL_OUT temperature was more than the CC2_B temperature but less than the CC2_T temperature. The highest operating temperature at 50 W was 112.3 °C. When the heat load of 70 W was applied, the temperature of the evaporator, the vapor line and the CC2 increased. But the LL_OUT temperature firstly went up to 58.2 °C and then dropped to 49.1 °C after about 2400 s, which was less than the temperature of the CC2_B and CC2_T. The temperature difference between CC2_T and CC2_B would increase with time. The final operating temperature at 70 W was 130.3 °C.

The reasons for the above temperature change can be expounded according to the following visualization results. The vapor–liquid distributions in th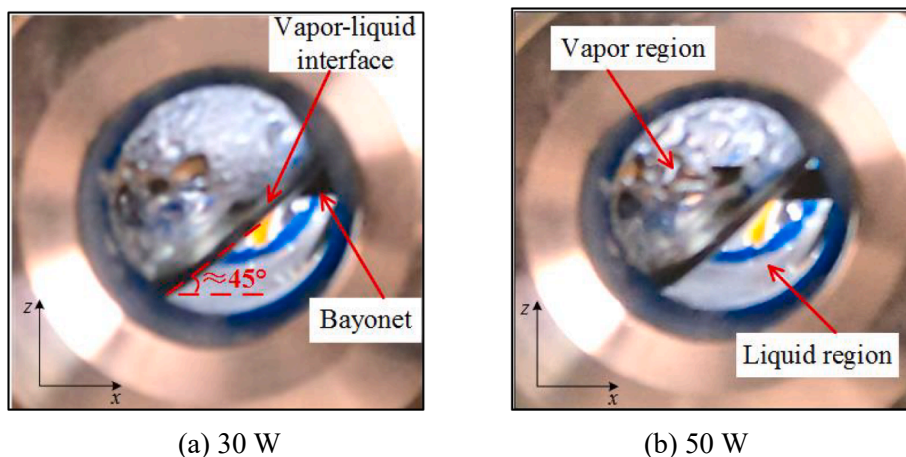e CC2 at 30 W and 50 W under direction A and 1 g are demonstrated in Fig. 5. Due to the acceleration force pointed to the CC1 from the CC2 under direction A, part of liquid in the CC2 and evaporator core was pushed into the CC1. Thus, most of the space inside CC1 was occupied by the liquid. However, most of the space inside CC2 would be filled with vapor. It can be seen from Fig. 5 that the vapor was much more than the liquid. The vapor–liquid interface formed an angle of 45° with the horizontal plane, which was caused by the combined action of the gravity and 1g acceleration force. The CC2 played the dominant role in controlling the temperature. Since the heat leak from the evaporator to the CCs, the temperature of the vapor in the CC2 was more than that of the liquid. Thus, the CC2_T temperature was higher than that of CC2_B.

According to Eq. (3), when the heat load increases, the mass flow rate of the working fluid also increases. Due to the large heat latent of water, the mass flow rate of the working fluid was small. Thus, the amount of the working fluid in the CCs was almost unchanged when the heat load increased from 30 W to 70 W. Furthermore, the increase of heat load could lead to the increase of the radial temperature difference of the wick and the temperature difference between the evaporator and CC. According to Eq. (5), both of the radial and axis heat leak increased. It would cause the CC2_T and CC2_B temperature increase, as shown in Fig. 4.

Moreover, obviously intermittent wave of the interface was also observed in the CC2 with heat loads of 50 W and 70 W. Fig. 6 presents the observed interface in the CC2 at different times for the case of 1 g and direction A with heat load of 70 W. It can be proved from Fig. 6 that the nucleate boiling occurred in the evaporator core along with the heat leak increase. As a result, bubbles were generated and local pressure increased. Due to the acceleration effect, some bubbles could be pushed into CC2. Therefore, the interface in the CC2 waved. Simultaneously, another partial bubbles could be pushed into the bayonet and reversely flow towards somewhere of the liquid line. It is believed that vapor–liquid two-phase slug flow formed in the liquid line and bayonet. The returning liquid near the wall flowed into the evaporator core. The same slug flow was observed by Cimbala et al. [36,37]. When the vapor with high temperature reached the LL_OUT point, the LL_OUT temperature rapidly went up. Moreover, the combination of the shell thermal conduction and the vapor heating in the CC2 made the LL_OUT temperature to be high. Due to the increase of the heat load caused the capillary pressure of the wick and the mass flow rate of the working fluid increasing. The returning liquid in the liquid line pushed the vapor–liquid interface to move downstream. As a result, the LL_OUT temperature reduced its magnitude after 2400 s. Finally, the evaporator temperature reached a constant value and the DCCLHP was at a steady-state condition.

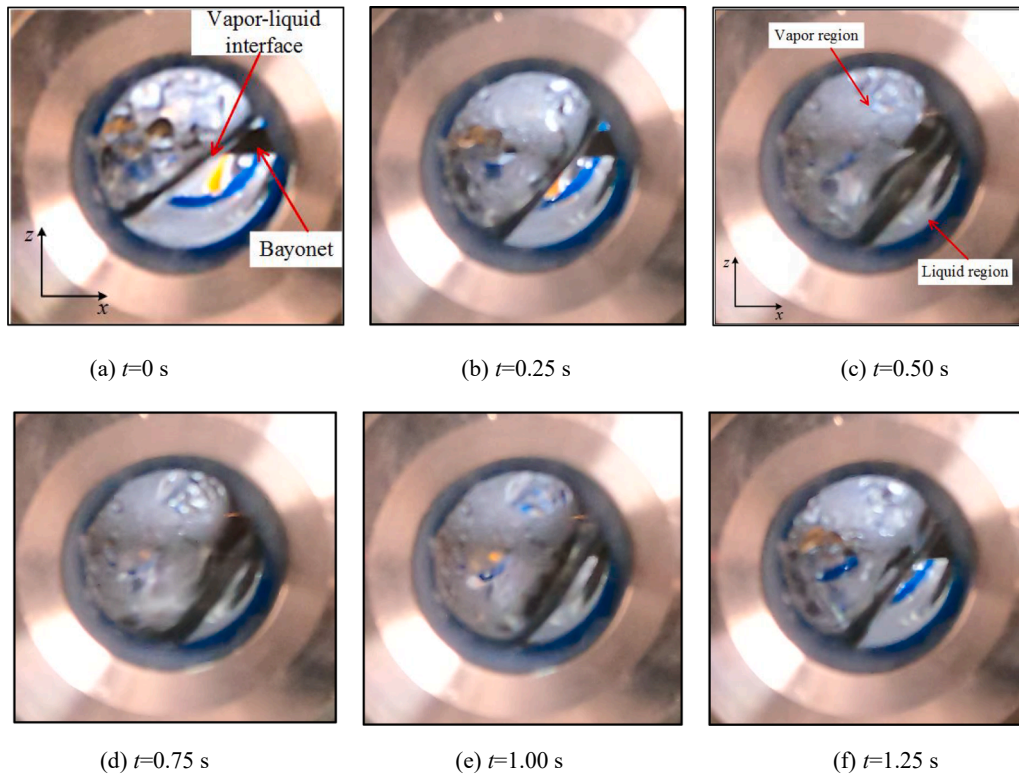Fig. 7 shows the temperature curves of the DCCLHP under 13 g and

(a) 30 W   (b) 50 W

Fig. 5. Vapor-liquid distribution inside CC2 at 1 g and direction A for 30 W and 50 W.

(a) t=0 s (b) t=0.25 s (c) t=0.50 s

(d) t=0.75 s (e) t=1.00 s (f) t=1.25 s

Fig. 6. Observed interface in the CC2 at different times at 1 g and direction A for 70 W.
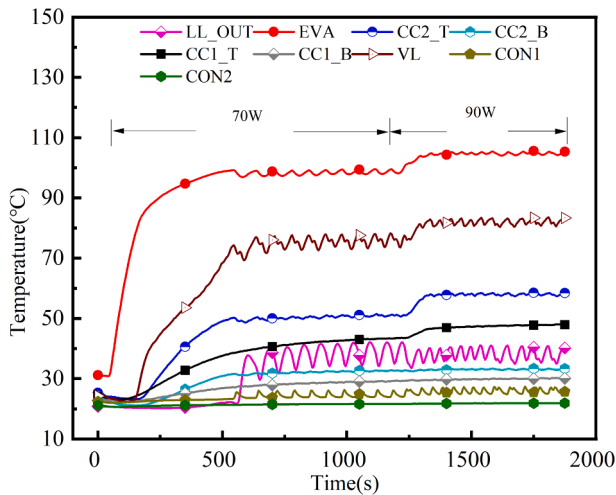

Fig. 7. Temperature curves of the DCCLHP at 13 g and direction B for 70 W and 90 W.

direction B with heat loads of 70 W and 90 W. It can be found from Fig. 7 that the evaporator temperature increased rapidly as the heat load of 70 W was applied. The VL temperature of the vapor line started to rise rapidly at approximate 150 s, which indicates that the vapor generated and entered the vapor line. Both the CC1_T and CC2_T temperature also obviously increased following the VL temperature. The CC1_B and CC2_B temperature increased slowly. When the evaporator temperature increased to 98 °C at about 500 s, the periodic oscillation of the loop temperature occurred. The amplitude of the LL_OUT temperature with 7.8 °C was the largest and the amplitudes of the vapor line and the evaporator were 6.6 °C and 2.4 °C. While the temperatures of the CC1 and the CON2 did not oscillate. Each component of the loop had the same period of 60 s.

When the heat load increased to 90 W, the temperatures of the EVA, CC1_T and CC2_T obviously increased. The evaporator temperature increased to approximate 104 °C. Compared to the case of 70 W, the amplitude and periodic of the temperature oscillation significantly decreased. The amplitudes of the LL_OUT, VL and EVA were 5.2 °C, 2.7 °C and 0.9 °C, respectively. The periodic was about 44 s.

During the temperature oscillation, it was observed that some small bubbles moved into the CC1 from the evaporator core, as shown in Fig. 8. Especially at 90 W, it can be clearly seen that the liquid working fluid carrying the bubbles and hot fluid flowed into the CC1. It indicates that the boiling very likely happened in the core. This phenomenon was similar to the results of Zhang et al. [12] under terrestrial gravity. It was believed that the boiling in the core could be easily observed as the LHP operated under acceleration condition. If the boiling in the core occurred, the heat leak from evaporator to CCs enlarged by the phase change heat transfer, which could increase the operating temperature of the DCCLHP.

The reason of above temperature oscillation can be addressed in terms of the visualization results of the condenser and CCs. The evaporator temperature went up rapidly after the heat load was applied. The heat leak from the evaporator to the CCs increased gradually. The nucleate boiling in the core happened as the heat leak increased to a certain value. Consequently, the temperature and pressure of the working fluid raised in the core. It led to the fluid with high temperature reversely flowed into the liquid line along the bayonet. It is speculated that the reverse flow was likely to be stratified flow. Thus, the LL_OUT temperature raised rapidly. Moreover, the reverse flow could be confirmed according to the vapor–liquid interface went backwards, as illustrated in Fig. 9. At this moment, the CON1 temperature went down. Due to the LL_OUT temperature increased, the subcooling of the returning liquid decreased, which could not balance the heat leak from the evaporator to the CCs according to Eq. (6).

Therefore, the temperature of the CCs and the evaporator increased. Accordingly, the temperature of the vapor line raised. The increased vapor pressure pushed the interface to move forward. Consequently, the
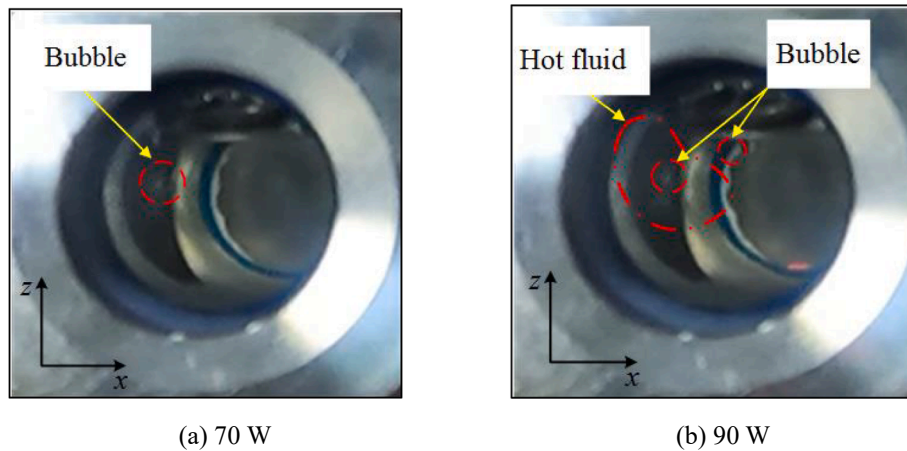
(a) 70 W

(b) 90 W

Fig. 8. Bubbles observed in the CC1 under 13 g and direction B for 70 W and 90 W.

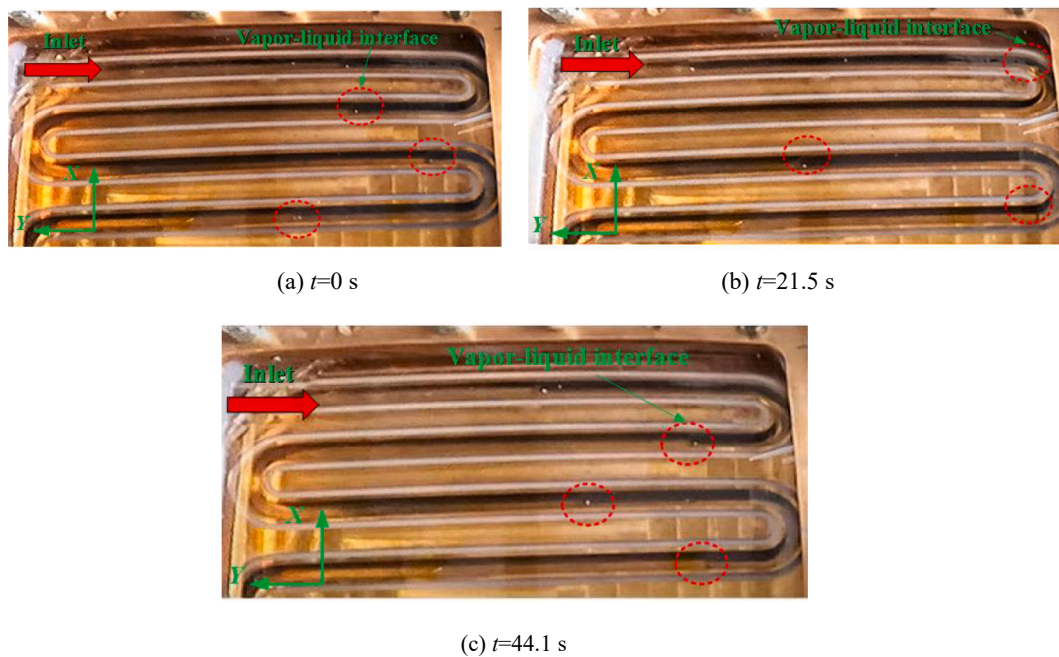(a) *t*=0 s

(b) *t*=21.5 s

(c) *t*=44.1 s

Fig. 9. Location of vapor–liquid interface in condenser at different times for 70 W and direction B.

temperature of the CON1 and LL_OUT decreased, which induced the subcooling of the returning liquid increase. The nucleate boiling in the core was not observed when the interface moved forward. The heat leak from the evaporator to the CCs decreased and the temperature of both CCs and evaporator reduced. Then the next oscillation cycle started. In addition, since the additional pressure resulted from the acceleration contributed to the returning of the liquid fluid, the acceleration effect could inhibit the deterioration of loop heat pipe performance caused by the boiling in the core.

3.2. Effect of acceleration direction

Fig. 10 presents the operating temperature and thermal conductance of the DCCLHP at both 5 g and 13 g under direction A and B. The corresponding results under gravity field are also presented in Fig. 10 for the reference. For direction A, due to the operating temperature at 110 W and 130 W exceeded 150 °C. The results were not presented in Fig. 10. It can be clearly seen from Fig. 10(a) that the operating temperature of the DCCLHP under gravity and direction A and B increased with the

increase of heat load. The operating temperature under direction A was obviously less than that under direction B at different heat loads, which was less than that under gravity. For the cases of 5 g, the operating temperature under direction A and B at 30 W was 86.8 °C and 71.6 °C, respectively. While the operating temperature at 90 W was 143.2 °C and 110 °C respectively. For direction B, the operating temperature at 5g and 110 W reached 142 °C. While it was 125.8 °C at 13 g and 130 W.

In Fig. 10(b), the thermal conductance of the DCCLHP increased generally with the increase of heat load, and the increasing tendency became small as the heat load is increased. It can be found that the thermal conductance under direction A was less than that under direction B except for the case of 30 W. While the thermal conductance under gravity was the smallest at each heat load. According to the operating temperature and thermal conductance, the performance of the DCCLHP under direction B was better than that under direction A. For the case of 90 W and 13 g, the operating temperature and thermal conductance under direction A were 136.9 °C and 1.02 W/K, respectively, while it was 104.5 °C and 1.48 W/K under direction B. The results indicated that the acceleration direction of direction B was more conducive to the
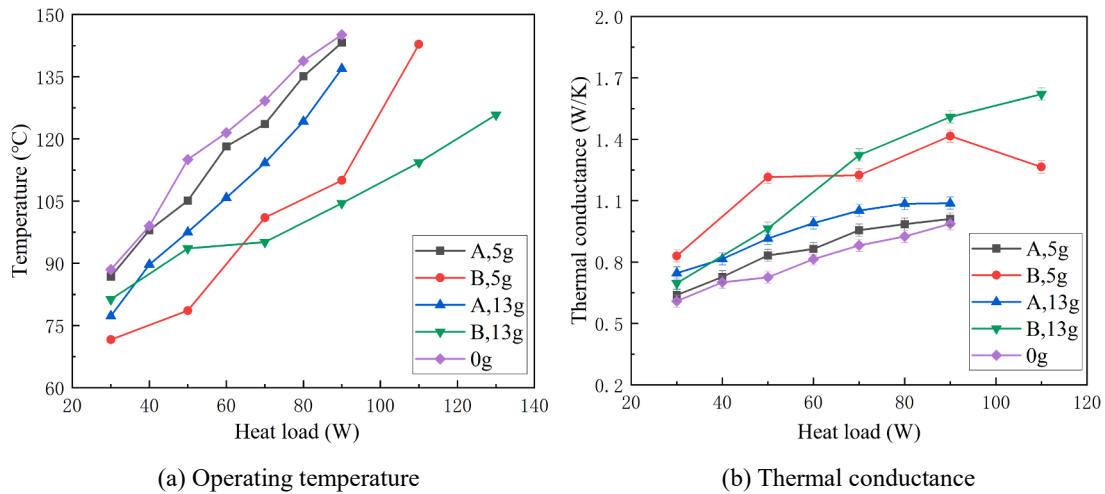
(a) Operating temperature   (b) Thermal conductance

Fig. 10. Operating characteristics for cases of direction A and B at 0 g, 5 g and 13 g.

DCCLHP operating in general. The reasons could be addressed as follows.

When the DCCLHP operated, the capillary pressure provided by the wick would be not less than Δp_{total} of the external loop determined by Eq. (1). Under the acceleration fields, the change of Δp_{VG} and Δp_{VL} caused by the acceleration effect could be neglected due to the vapor density was small. The change of Δp_W and $\Delta p_{CON}^{2\varphi}$ could also be neglected since the length was small. Due to large liquid density, the additional pressure resulted from the acceleration force on the liquid line, condenser and bayonet could change Δp_{total} according to Eq. (2). Accordingly, the capillary pressure would be changed to balance Δp_{total}. Under direction A, the acceleration force would become a flow resistance in the condenser as long as the vapor–liquid interface did not locate somewhere of the last straight pipe of the condenser. It would prevent the subcooled liquid from flowing back to the CCs. However, the additional pressure resulted from the acceleration force became the driven force in the bayonet. Moreover, the flow resistance was smaller than the driven force in the bayonet due to the larger length of bayonet than the length of condenser along the acceleration direction. Therefore,

the acceleration effect would reduce Δp_{total}.

Under direction B, the location of the vapor–liquid interface in the condenser determined the additional pressure of the liquid in the condenser by the acceleration effect. However, the visualization results showed that the vapor–liquid distribution in the condenser under direction B was obviously different from that under direction A. Fig. 11 presented that the distributions at 13 g and direction B with the heat loads of 30 W and 130 W. It is clear that the liquid was mainly accumulated in the channels near the left U-bends by the acceleration effect. While the vapor was distributed near the right U-bends. And they were divided into multiple segments and distributed alternately. Considering the condensation of the condenser, a thin liquid layer could be formed at the bottom of the channels and stratified flow existed in the vapor zone. When the heat load was 30 W, the interface was not observed at the outlet of the condenser, as shown in Fig. 11(a). it can be inferred that the interface would locate somewhere along the liquid line. For the case of 130 W, the interface located near the outlet of the condenser, as shown in Fig. 11(b), which indicated that the liquid line filled the subcooled liquid. The acceleration direction was the same as the flow direction of
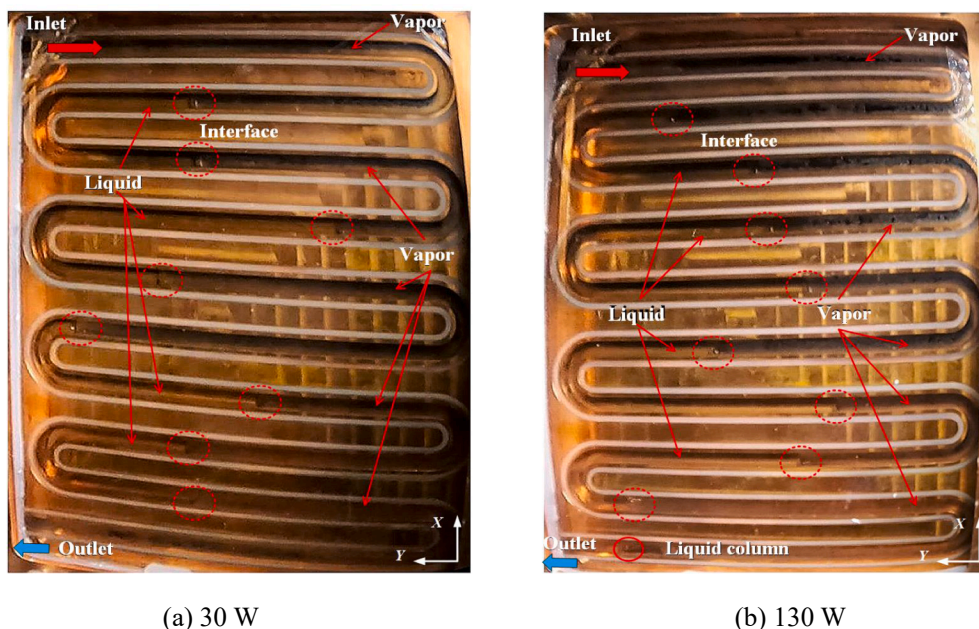

(a) 30 W   (b) 130 W

Fig. 11. Vapor-liquid distribution in the condenser at 30 W and 130 W under 13 g and direction B.

the liquid in the liquid line. Although the additional pressure resulted from the acceleration could became the flow resistance in the condenser, the total additional pressure would significantly reduce Δp_{total}. As a consequence, the acceleration effect under direction B could contribute more to the DCCLHP compared to that under direction A.

3.3. Effect of acceleration magnitudes

It is noted that different acceleration magnitudes can lead to the working fluid to be subjected to different forces. Therefore, the DCCLHP presented different operating temperature and thermal conductance. Fig. 12 showed the steady-state operating temperature and thermal conductance versus the acceleration magnitude under directions A and B at different heat loads, respectively. For the cases at direction A shown in Fig. 12(a) and (b), the operating temperature profiles revealed a trend of gradual decrease as the acceleration increased from 1 g to 13 g. While the thermal conductance profiles showed a trend of gradual increase. It can be found at 70 W that the operating temperature and thermal conductance were 130.3 °C and 0.90 W/K at 1 g. They were 113.8 °C and 1.05 W/K at 13 g, respectively. It is believed that the large acceleration magnitude was conducive to the DCCLHP operating. However, when the acceleration increased to 15 g, the operating temperature was higher than that at 13 g and the thermal conductance was less than that at 13 g. The reasons for this phenomenon could be explained as follows.

When the acceleration increased to 15 g for direction A, the

acceleration effect could significantly change the vapor–liquid distribution in the loop. Most of the liquid in the CC2 was pushed into the CC1 and the vapor occupied most of the space of the CC2 and a part of the space of the core. This vapor–liquid distribution could significantly increase the heat leak from the evaporator to the CC2 and decrease the heat leak to the CC1. Moreover, the liquid working fluid was not able to wet part of the wick near the CC2 due to acceleration effect. The local region of the wick was likely to dry out due to the liquid could not be supplied and formed the local wick dryout. The speculative vapor–liquid distribution and local wick dryout are shown in Fig. 13. The local wick dryout was observed by Cimbala et al. [36] under gravity field. The vapor with high temperature and pressure in the vapor groove would penetrate the wick and enter into the core and the CC2. If the acceleration became larger, the wick would be dryout by the acceleration effect and further caused the DCCLHP could not operate normally.

In the current experiment, the phenomenon of the intermittent spattering of liquid drop was observed in the CC2 at 70 W and 15g under direction A, as shown in Fig. 14. In Fig. 14(a), two liquid drops were observed to be spattered from the core into the CC2 within approximate 0.02 s. In Fig. 14(b), a liquid drop was spattered firstly from the core and then the second liquid drop appeared following the first liquid drop within about 0.02 s. The observation indicated that the superheated vapor entered into the liquid in the core and further drove the liquid spattering into the CC2 in form of liquid drops. The heat leak from the evaporator to the CC2 enlarged. Therefore, the temperature of the CC2
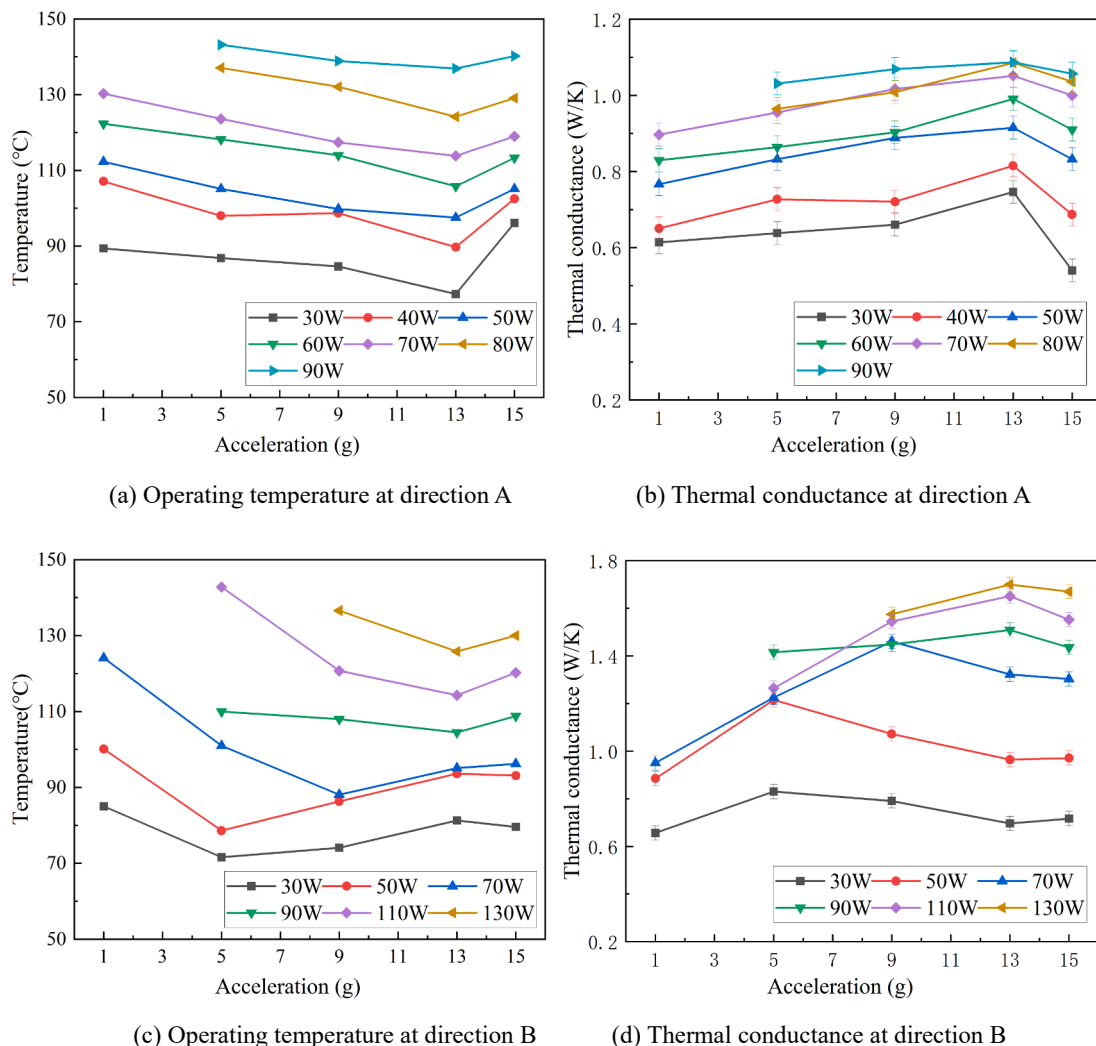

(a) Operating temperature at direction A

(b) Thermal conductance at direction A

(c) Operating temperature at direction B

(d) Thermal conductance at direction B

Fig. 12. Operating temperature and thermal conductance of the DCCLHP at different acceleration magnitudes for directions A and B and different heat loads.
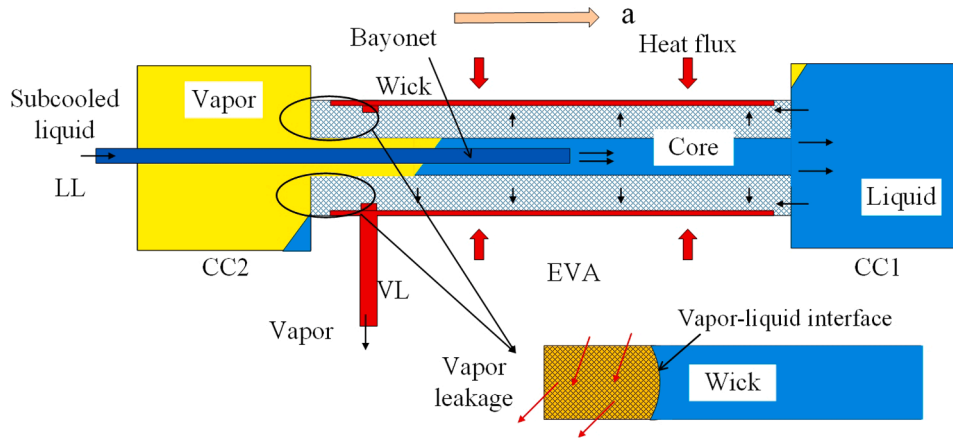
Fig. 13. Speculative vapor–liquid distribution and local wick dryout at 15 g and direction A.

(a) Location of spattered liquid drops from 0 s to 0.017 s

(b) Location of another spattered liquid drops from 0 s to 0.017 s
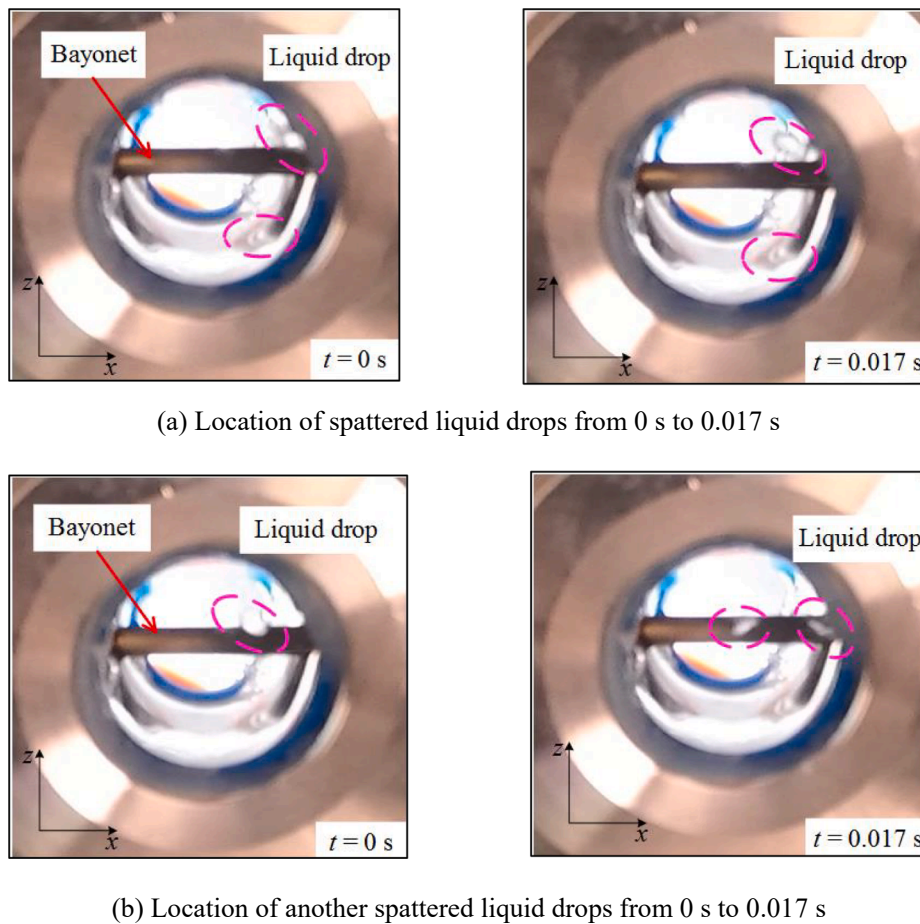
Fig. 14. Intermittent spattering of liquid drop in the CC2 at 70 W, 15 g and direction A.

and EVA increased.

For the cases of direction B shown in Fig. 12(c) and (d), as the acceleration magnitude increased to 13 g, the operating temperature of the DCCLHP firstly decreased and then increased. But the thermal conductance presented an opposite variation behavior. The transition acceleration, that is the acceleration magnitude corresponding to the minimum temperature or the maximum thermal conductance, showed different values with different heat loads. For the cases of 30 W and 50 W, the transition acceleration was 5 g, whereas it was 9 g for the cases of 70 W. For the cases of 90 W, 110 W and 130 W, it increased to 13 g.

When the acceleration magnitude increased from 13 g to 15 g, the operating temperature at 30 W and 50 W reduced slightly and the thermal conductance increased slightly. For the cases of 70 W to 130 W, the operating temperature increased and the thermal conductance reduced. For the case of 5 g and 110 W, the operating temperature reached the maximum value of 142.8 °C. The minimum temperature of 71.6 °C was at 5 g and 30 W. However, at 13 g and 130 W, the maximum thermal conductance of 1.70 W/K is reached. The minimum thermal conductance of 0.65 W/K was found at 1 g and 30 W.

The reasons causing above variation of the operating temperature

versus the acceleration could be explained as follows. Under direction B at 30 W, the vapor–liquid distribution in the evaporator and CCs was similar to that in gravity. The vapor–liquid interface formed an angle with the horizontal plane under the combined action of the acceleration force and gravity. Compared to the case in gravity, the heat leak from the evaporator to the CCs would not change. However, the acceleration effect contributed to the returning of the liquid. According to Eqs. (1) and (2), the additional pressure resulted from the acceleration increased as the acceleration increased from 1g to 5g, so Δp_{total} decreased. According to Eq. (7), the operating temperature reduced.

When the acceleration increased from 5 g to 13 g, the liquid line could include the vapor due to the mass flow rate was small at 30 W. Moreover, the large acceleration could result in the large additional pressure, a little of the liquid in the liquid line could be squeezed into the CCs. Consequently, the length of the liquid column reduced with the increase of acceleration. Δp_{total} increased due to the comprehensive effect of acceleration increase and the liquid column decrease. Therefore, the operating temperature raised. When the acceleration increased from 13 g to 15 g, the length of the liquid column in the liquid line could change slightly. But the increase of the acceleration magnitude could lead to Δp_{total} decreased. Thus, the operating temperature went down.

When the heat load increased, the mass flow rate of the working fluid enlarged in the loop, so Δp_{total} increased. According to Eq. (2), the additional pressure resulted from the acceleration was kept constant since it was independent with the mass flow rate. Consequently, the ratio of the additional pressure caused by the acceleration in the total pressure drop would reduce. Therefore, the larger acceleration was needed to produce the higher additional pressure to balance the total flow resistance. In other words, the larger the heat load, the greater the transition acceleration. In addition, it is worthy to note that for each acceleration magnitude, the operating temperature and thermal conductance generally increased with the heat load increasing.

4. Conclusions

In the current work, a nickel-water DCCLHP with visual CCs and condenser was designed and manufactured. The impacts of several control parameters such as heat load, acceleration magnitude and direction on the operating performance of the DCCLHP was analyzed in a systematic manner. The major conclusions are summarized as follows:

(1) The operating temperature increases with the increase of heat load under both directions A and B. For the case of direction A, it is observed that the CC2 was in vapor–liquid two-phase state. The amount of vapor increased and the vapor–liquid interface showed wave with the increase of heat load. Under direction B, temperature oscillation occurred at 70 W and 90 W at 13 g. During temperature oscillation, bubbles appeared in the CC1 and the vapor–liquid interface moved back and forth in the condenser. The reason for oscillation was the combined action of the boiling in the core and the acceleration effect.

(2) The operating temperature under direction A was higher than that under direction B. The thermal conductance was less than that under direction B. The acceleration effect under direction B generally improved the DCCLHP operating performance. The maximum operating temperature was 143.2 °C at 5 g with heat load of 90 W under direction A. While the minimum operating temperature was 71.6 °C at 5 g for 30 W under direction B. The maximum thermal conductance was 1.70 W/K at 13 g and 130 W under direction B. While the minimum thermal conductance was 0.54 W/K at 15 g and 30 W under direction A.

(3) As the acceleration increased from 1 g to 15 g, the operating temperature initially decreased and then increased. While the thermal conductance firstly increased and then decreased in general for direction A. The transition acceleration was 13 g. For direction B, the operating temperature and thermal conductance

showed similar change trend except for the cases of 30 W and 50 W. The transition acceleration increased with the increase of heat load.

(4) It was observed that liquid drops intermittently spattered in the CC2 at 15 g under direction A. The acceleration effect under direction B made multiple segments of the liquid and vapor phase alternately distribute in the U-bends zone on both sides of the condenser. Stratified flow formed in the condenser.

In the current work, we demonstrated the two-phase flow and heat transfer behaviors in the DCCLHP under acceleration fields by visual observation, which are essential for the design and performance assessing of the DCCLHP system under acceleration fields. The relevant analysis and heat transfer mechanism explanation were proposed for the first time. This study paved a foundation to solve the critical problems of the DCCLHP. Establishing the model of flow and heat transfer and further investigating operational performance of the DCCLHP under acceleration fields are the focus of our future work.

Declaration of Competing Interest

The authors declare that they have no known competing financial interests or personal relationships that could have appeared to influence the work reported in this paper. No potential conflict of interest was reported by the authors.

Data availability

Data will be made available on request.

References

[1] H. Lv, H. Ma, N. Mao, T. He, Boiling heat transfer mechanism of environmental-friendly refrigerants: A review, Int. J. Refrig. 133 (2022) 214–225.
[2] S.A. Nada, R.M. El-Zoheiry, M. Elsharnoby, O.S. Osman, Enhancing the thermal performance of different flow configuration minichannel heat sink using Al_2O_3 and CuO- water nanofluids for electronic cooling: An experimental assessment, Int. J. Therm. Sci. 181 (2022), 107767.
[3] Y.F. Maydanik, S.V. Vershinin, M.A. Chernysheva, Loop heat pipes, Appl. Therm. Eng. 25 (5–6) (2005) 635–657.
[4] K. Xiong, L. Meng, S. Wang, Design, fabrication, investigation and analysis of a novel flat evaporator loop heat pipe for cooling high heat flux server chips, Appl. Therm. Eng. 201 (2022), 117775.
[5] H.F. Wang, G.P. Lin, L.Z. Bai, Y.B. Tao, D.S. Wen, Comparative study of two loop heat pipes using R134a as the working fluid, Appl. Therm. Eng. 164 (2020), 114459.
[6] Y. Aono, N. Watanabe, A. Ueno, H. Nagano, Development of a loop heat pipe with kW-class heat transport capability, Appl. Therm. Eng. 183 (2021), 116169.
[7] L. Liu, B. Yuan, C. Cui, X. Yang, J. Wei, Investigation of a loop heat pipe to achieve high heat flux by incorporating flow boiling, Int. J. Heat Mass Transf. 195 (2022), 123173.
[8] Y. Chen, M. Groll, R. Mertz, Y.F. Maydanik, S.V. Vershinin, Steady-state and transient performance of a miniature loop heat pipe, Int. J. Therm. Sci. 45 (2006) 1084–1090.
[9] J. Ku, L. Ottenstein, P. Rogers, K. Cheung. Investigation of low power operation in a loop heat pipe, in: 31st International Conference On Environmental Systems, 2001.
[10] T. Kaya, J. Ku, Thermal operational characteristics of a small-loop heat pipe, J. Thermophys. Heat Transfer 17 (2003) 464–470.
[11] A.J. Fleming, S.K. Thomas, K.L. Yerkes, Titanium-water loop heat pipe operating characteristics under standard and elevated acceleration fields, J. Thermophys. Heat Transfer 24 (2010) 184–198.
[12] K. Yerkes, J. Scofield, D. Courson, H. Jiang, An experimental investigation into the transient performance of a titanium-water loop heat pipe subjected to a steady-periodic acceleration field, in: 50th AIAA Aerospace Sciences Meeting including the New Horizons Forum and Aerospace Exposition, 2012, 1009.
[13] D. Gluck, C. Gerhart, S. Stanley, Characterization of a high capacity, dual compensation chamber loop heat pipe. AIP Conference Proceedings, Am. Instit. Phys. 458 (1) (1999) 943–948.
[14] C. Gerhart, D. Gluck, Summary of operating characteristics of a dual compensation chamber loop heat pipe in gravity, in: 11th International Heat Pipe Conference, Tokyo, Japan, 1999.
[15] G. Lin, H. Zhang, X. Shao, J. Cao, T. Ding, J. Miao, Development and test results of a dual compensation chamber loop heat pipe, J. Thermophys. Heat Transfer 20 (2006) 825–834.

[16] L. Bai, G. Lin, D. Wen, J. Feng, Experimental investigation of startup behaviors of a dual compensation chamber heat pipe with insufficient fluid inventory, Appl. Therm. Eng. 29 (2009) 1447–1456.

[17] L. Bai, Y. Tao, Y. Guo, G. Lin, Startup characteristics of a dual compensation chamber loop heat pipe with an extended bayonet tube, Int. J. Heat Mass Transf. 148 (2020), 119066.

[18] L. Bai, J. Fu, L. Pang, Y. Tao, G. Lin, D. Wen, Experimental study on a dual compensation chamber loop heat pipe with dual bayonet tubes, Appl. Therm. Eng. 180 (2020), 115821.

[19] Y.Q. Xie, Y. Zhou, D.S. Wen, H.W. Wu, G. Haritos, H.X. Zhang, Experimental investigation on transient characteristics of a dual compensation chamber loop heat pipe subjected to acceleration forces, Appl. Therm. Eng. 130 (2018) 169–184.

[20] L.Z. Han, Y.Q. Xie, J.Q. Zhu, H.W. Wu, H.X. Zhang, Experimental and analytical study of dual compensation chamber loop heat pipe under acceleration force assisted condition, Int. J. Heat Mass Transf. 153 (2020), 119615.

[21] T. Kaya, T.T. Hoang, Mathematical modeling of loop heat pipes and experimental validation, J. Thermophys. Heat Transfer 13(1999) 314–320.

[22] S. Launay, M. Vallée, State-of-the-art experimental studies on loop heat pipes, Front. Heat Pipes (FHP) 2 (1) (2011).

[23] S. He, P. Zhou, W. Liu, Z. Liu, Experimental study on thermal performance of loop heat pipe with a composite-material evaporator for cooling of electronics, Appl. Therm. Eng. 168 (2020), 114897.

[24] Y.F. Maydanik, S.V. Vershinin, M.A. Chernysheva, Comparison tests of loop heat pipes with flat evaporators of different types, Int. J. Heat Mass Transf. 186 (2022), 122491.

[25] M.A. Chernysheva, Y.F. Maydanik, Numerical simulation of transient heat and mass transfer in a cylindrical evaporator of a loop heat pipe, Int. J. Heat Mass Transf. 51 (2008) 4204–4215.

[26] B. Siedel, V. Sartre, F. Lefèvre, Numerical investigation of the thermohydraulic behaviour of a complete loop heat pipe, Appl. Therm. Eng. 61 (2013) 541–553.

[27] M.A. Chernysheva, Y.F. Maydanik, Simulation of heat and mass transfer in a cylindrical evaporator of a loop heat pipe, Int. J. Heat Mass Transf. 131 (2019) 442–449.

[28] T. Adachi, X. Chang, H. Nagai, Numerical analysis of loop heat pipe using nucleate boiling model in evaporator core, Int. J. Heat Mass Transf. 195 (2022), 123207.

[29] R. Singh, A. Akbarzadeh, C. Dixon, M. Mochizuki, Theoretical modelling of miniature loop heat pipe, Heat Mass Transf. 46 (2009) 209–224.

[30] L. Bai, G. Lin, H. Zhang, D. Wen, Mathematical modeling of steady-state operation of a loop heat pipe, Appl. Therm. Eng. 29 (2009) 2643–2654.

[31] B. Siedel, V. Sartre, F. Lefèvre, Literature review: Steady-state modelling of loop heat pipes, Appl. Therm. Eng. 75 (2015) 709–723.

[32] C.Y. Weng, T.S. Leu, Two-phase flow pattern based theoretical study of loop heat pipes, Appl. Therm. Eng. 98 (2016) 228–237.

[33] M. Gürü, A. Sözen, U. Karakaya, E. Çiftçi, Influences of bentonite-deionized water nanofluid utilization at different concentrations on heat pipe performance: An experimental study, Appl. Therm. Eng. 148 (2019) 632–640.

[34] D. Yılmaz Aydın, E. Çiftçi, M. Gürü, A. Sözen, The impacts of nanoparticle concentration and surfactant type on thermal performance of a thermosyphon heat pipe working with bauxite nanofluid, Energy Sources, Part A: Recovery, Utiliz., Environ. Effects 43 (2021) 1524-1548.

[35] D.Y. Aydın, M. Gürü, A. Sözen, E. Çiftçi, Thermal Performance Improvement of the Heat Pipe by Employing Dolomite/Ethylene Glycol Nanofluid, Int. J. Renew. Energy Develop. 9 (1) (2020).

[36] J.M. Cimbala, J.S. Brenizer, A.P.Y. Chuang, S. Hanna, C.T. Conroy, A.A. El-Ganayni, D.R. Riley, Study of a loop heat pipe using neutron radiography, Appl. Radiat. Isot. 61 (2004) 701–705.

[37] P.Y.A. Chuang, J.M. Cimbala, J.S. Brenizer, Experimental and analytical study of a loop heat pipe at a positive elevation using neutron radiography, Int. J. Therm. Sci. 77 (2014) 84–95.

[38] A. Okamoto, R. Hatakenaka, M. Murakami, Visualization of a loop heat pipe using neutron radiography, Heat Pipe Sci. Technol., Int. J. 2 (1–4) (2011).

[39] R. Hatakenaka, A. Okamoto, Y. Mase, M. Murakami, H. Iikura, Visualization of internal fluid behavior in a miniature loop heat pipe using neutron radiography, in: 41st International Conference on Environmental Systems, 2011, 5140.

[40] G. Lin, N. Li, L. Bai, D. Wen, Experimental investigation of a dual compensation chamber loop heat pipe, Int. J. Heat Mass Transf. 53 (2010) 3231–3240.

[41] M. Zhang, Z.L. Liu, G.Y. Ma, S.Y. Cheng, Numerical simulation and experimental verification of a flat two-phase thermosiphon, Energy Convers. Manage. 50 (4) (2009) 1095–1100.

[42] X. Wang, J. Wei, Visual investigation on startup characteristics of a novel loop heat pipe, Appl. Therm. Eng. 105 (2016) 198–208.

[43] Y. Yang, K. Zhu, Y.B. Wang, J. Wei, M.Z. Zheng, Z. Cui, Experimental investigation and visual observation of a vapor-liquid separated flat loop heat pipe evaporator, Appl. Therm. Eng. 101 (2016) 71–78.

[44] Y. Zhao, S. Chang, B. Yang, W. Zhang, M. Leng, Experimental study on the thermal performance of loop heat pipe for the aircraft anti-icing system, Int. J. Heat Mass Transf. 111 (2017) 795–803.

[45] Q. Su, S.N. Chang, M.J. Song, Y.Y. Zhao, C.B. Dang, An experimental study on the heat transfer performance of a loop heat pipe system with ethanol-water mixture as working fluid for aircraft anti-icing, Int. J. Heat Mass Transf. 139 (2019) 280–292.

[46] M. Nishikawara, K. Otain, Y. Ueda, Liquid-vapor phase behavior and operating characteristics of the capillary evaporator of a loop heat pipe at start-up, Int. J. Therm. Sci. 129 (2018) 426–433.

[47] Y. Yamamda, M. Nishikawara, H. Yanada, Y. Ueda, Predicting the performance of a loop heat pipe considering evaporation from the meniscus at the three-phase contact line, Therm. Sci. Eng. Progr. 11 (2019) 125–132.

[48] Q.D. Zhang, G.P. Lin, X.B. Shen, L.Z. Bai, D.S. Wen, Visualization study on the heat and mass transfer in the evaporator-compensation chamber of a loop heat pipe, Appl. Therm. Eng. 164 (2020), 114472.

[49] G.E. Achkar, P. Lavieille, M. Miscevic, Loop heat pipe and capillary pumped loop design: About heat transfer in the isolated bubbles zone of condensers, Appl. Therm. Eng. 33 (2012) 253–257.

[50] E. Bartuli, S. Vershinin, Y.F. Maydanik, Visual and instrumental investigations of a copper–water loop heat pipe, Int. J. Heat Mass Transf. 61 (2013) 35–40.

[51] X. Chang, N. Watanabe, H. Nagano, Visualized study of the gravitational effect in a loop heat pipe with two evaporators and one condenser, International Heat Transfer Conference Digital Library, Begel House Inc., 2018.

[52] X. Chang, N. Watanabe, H. Nagano, Visualization study of a loop heat pipe with two evaporators and one condenser under gravity-assisted condition, Int. J. Heat Mass Transf. 135 (2019) 378–391.

[53] G. Zhou, L. Ji, Two-phase flow characteristics of a high performance loop heat pipe with flat evaporator under gravity, Int. J. Heat Mass Transf. 117 (2018) 1063–1074.

[54] K.F. Yan, N.X. Li, R.Z. Zhao, Y.N. Wu, R.J. Xie, Visualization study on the condensation in a propylene loop heat pipe operating at condenser temperatures between 153 and 283 K, Appl. Therm. Eng. 185 (2021), 116349.

[55] K.F. Yan, R.Z. Zhao, N.X. Li, G.M. Xu, Y.N. Wu, Experimental investigation and visualization study of the condensation characteristics in a propylene loop heat pipe, J. Therm. Sci. 30 (5) (2021) 1803–1813.

[56] J. Ku, L. Ottenstein, T. Kaya, P. Rogers, C. Hoff, Testing of a loop heat pipe subjected to variable accelerating forces, Part 1: Start-up, in: 11th Annual Spacecraft Thermal Control Technology Workshop, California, America, 2000.

[57] J. Ku, L. Ottenstein, T. Kaya, P. Rogers, Testing of a loop heat pipe subjected to variable accelerating forces, Part 2: Temperature stability, in: 11th Annual Spacecraft Thermal Control Technology Workshop. California, America, 2000.

[58] K.L. Yerkes, J.D. Scofield, D.L. Courson, H. Jiang, Steady-periodic acceleration effects on the performance of a loop heat pipe, J. Thermophys. Heat Transfer 28 (3) (2014) 440–454.

[59] K.L. Yerkes, J. Scofield, D. Courson, Performance of a loop heat pipe subjected to a phase-coupled heat input to an acceleration field, in: 46th AIAA Thermophysics Conference, 2016, 4145.

[60] Y.Q. Xie, X.Y. Li, S.J. Dong, H.X. Zhang, H.W. Wu, Experimental investigation on operating behaviors of loop heat pipe with thermoelectric cooler under acceleration conditions, Chin. J. Aeronaut. 33 (03) (2020) 852–860.

[61] Y.Q. Xie, X.Y. Li, L.Z. Han, J.Q. Zhu, H. Gao, D.S. Wen, Experimental study on operating characteristics of a dual compensation chamber loop heat pipe in periodic acceleration fields, Appl. Therm. Eng. 176 (2020), 115419.

[62] Z. Fang, Y. Xie, Y. Xu, H. Wu, H. Zhang, L. Han, Performance investigation of a loop heat pipe integrated with thermoelectric cooler under acceleration field, Int. J. Heat Mass Transf. 178 (2021), 121476.

[63] K.H. Le, A. Kharaghani, C. Krisch, E. Tsotsas, Pore network simulations of heat and mass transfer inside an unsaturated capillary porous wick in the dry-out regime, Transp. Porous Media 114 (3) (2016) 623–648.

[64] H. Jouhara, R. Meskimmon, An investigation into the use of water as a working fluid in wraparound loop heat pipe heat exchanger for applications in energy efficient HVAC systems, Energy 156 (2018) 597–605.

[65] Y. Maydanik, V. Pastukhov, M. Chernysheva, Development and investigation of a loop heat pipe with a high heat-transfer capacity, Appl. Therm. Eng. 130 (2018) 1052–1061.

[66] R.J. Moffat, Describing uncertainties in experimental results, Exp. Therm Fluid Sci. 1 (1988) 3–17.